https://doi.org/10.5194/egusphere-2026-2197
Preprint. Discussion started: 23 April 2026
© Author(s) 2026. CC BY 4.0 License.

From opportunity to continuity: A CubeSat implementation to enhance Earth's radiation budget observations from space

McKenzie A. Hawkins[1,2], Matthew Watwood[1,2], Mathew van den Heever[1,3], Peter Pilewskie[1,2], Dave Harber[1]

[1]Laboratory for Atmospheric and Space Physics, Boulder, 80303, United States of America
[2]Department of Atmospheric and Oceanic Sciences, University of Colorado Boulder, Boulder, 80303, United States of America
[3]Department of Aerospace Engineering, University of Colorado Boulder, Boulder, 80303, United States of America

Correspondence to: McKenzie A. Hawkins (mckenzie.hawkins@lasp.colorado.edu)

Abstract. Earth's radiation budget (ERB) is an essential climate variable, and its continuous observation from space is critical to understanding long-term climate change. The Clouds and Earth's Radiant Energy System (CERES) has maintained the longest continuous ERB record since 2000, with its follow-on mission, Libera, launching in 2027 with a 5-year prime mission lifetime. Beyond Libera, plans for ERB continuity remain uncertain, increasing the possibility of future gaps in the record. The Compact Total Irradiance Monitor (CTIM) was a 6U CubeSat developed under the NASA In-Space Validation of Earth Science Technologies (InVEST) program to measure total solar irradiance (TSI). Launched in July 2022 and operating until November 2023, CTIM collected climate-quality science at an uncertainty of 0.017%. During orbital eclipse, CTIM was pointed in the nadir direction to measure Earth's outgoing longwave emission, exploring the Earth-observing potential of an instrument designed for TSI. These measurements were compared to coincident CERES observations aboard Terra, Aqua, and NOAA-20. Additional adjustment factors for limb darkening were derived from radiative transfer simulations over a variety of scene types and atmospheric conditions and applied to CERES non-nadir viewing observations to better match the CTIM nadir observations and explain some of the variance exhibited between measurements. The resulting comparisons show an overall relative agreement of 1.3%, within respective instrument uncertainties. This study demonstrates that leveraging CubeSat technology could complement heritage ERB missions and reduce the risk of future observation gaps. The routine inclusion of Earth-viewing capabilities in future TSI instrument designs represents a natural extension of this work, with the potential to meaningfully contribute to ERB observation continuity and reduce dependence on dedicated large-scale missions.

1 Introduction

The Earth's Radiation Budget (ERB) characterizes the flow of radiative energy from the Sun into the Earth system and out of the system as reflected solar (shortwave) and emitted terrestrial (longwave) radiation. The system is in equilibrium when the difference between incoming and reflected solar radiation, or absorbed solar radiation, is balanced by the emitted terrestrial

https://doi.org/10.5194/egusphere-2026-2197
Preprint. Discussion started: 23 April 2026
© Author(s) 2026. CC BY 4.0 License.

radiation (Loeb et al., 2016; Stephens et al., 2012; von Schuckmann et al., 2016). Imbalances in the radiation budget arise due to climate forcings, feedback mechanisms, and internal variability (Forster et al., 2021; Loeb et al., 2024). The energy exchanges driven by these factors are represented in the ERB, making it a fundamental quantity for monitoring global climate change: when Earth absorbs more (less) energy than it emits over time, global mean surface temperature increases (decreases), as the climate system adjusts toward equilibrium (Loeb et al., 2018b; von Schuckmann et al., 2023). Larger departures from equilibrium trigger amplified responses to restore balance, and the resulting changes are manifested in the ERB on decadal-to-centennial timescales (Barkstrom & Smith, 1986; Dewitte & Clerbaux, 2018). Because the ERB responds over decadal-to-centennial timescales, accurate and continuous monitoring of incoming and outgoing radiation is essential for understanding climate change. These long-term observations not only illuminate the mechanisms driving climate shifts but also help inform mitigation strategies for managing future climate risks.

Both the Intergovernmental Panel on Climate Change (IPCC) (Forster et al., 2021) and the most recent Earth Decadal Survey (National Academies of Sciences, 2018) designate ERB observations as essential for determining the current energy imbalance and predicting future climate. Moreover, the ERB is designated as an Essential Climate Variable (ECV) by the Global Climate Observing System (GCOS), operating under the coordination of the World Meteorological Organization (WMO), emphasizing the necessity for continuous, accurate monitoring of Earth's radiative energy (Global Climate Observing System, 2023).

Since the 1950s, satellite missions have provided essential observations of the ERB on a global scale (House et al., 1986). The Clouds and the Earth's Radiant Energy System (CERES) instruments began the longest continuous record of Earth's radiative energy system, extending from 2000 to the present (CERES first flew on Tropical Rainfall Measuring Mission [TRMM] in the late 1990s, without global coverage or data continuation through 2000; Loeb et al., 2024; Minnis et al., 2023). To ensure the continuation of the record, NASA's first Earth Venture Continuity mission, Libera, will provide seamless overlap and continuity of ERB observations with CERES in 2027 (Pilewskie et al., 2022).

Six CERES instruments currently operating aboard four satellites—Flight Model-1 (FM-1) and FM-2 on Terra, FM-3 and FM-4 on Aqua, FM-5 on Suomi-National Polar-Orbiting Partnership (S-NPP), and FM-6 on NOAA-20—have provided over 26 years of measurements of reflected solar radiation and emitted longwave radiation, delivering state-of-the-art, continuous observations of Earth's radiative energy budget (Priestely et al., 2018; Su et al., 2020). Despite this success, sustaining the ERB record faces increasing challenges. As the CERES instruments on Terra and Aqua near the end of their operational lives in 2026, and potentially S-NPP in 2027, it is likely that CERES FM-6 aboard NOAA-20 will be the only instrument to overlap with Libera when it launches on Joint Polar Satellite System-4 (JPSS-4) in late 2027 (Loeb et al., 2024). Libera reaches its prime mission end-of-lifetime by 2033, with no planned ERB missions to follow. From this operational timeline, Loeb et al. (2024) determine that as the number of ERB instruments decrease from four to one in just six years, the estimated

https://doi.org/10.5194/egusphere-2026-2197
Preprint. Discussion started: 23 April 2026
© Author(s) 2026. CC BY 4.0 License.

probability of an ERB data gap reaches 33% by 2028 and rises to 60% by 2035 if Libera remains operational. Loeb et al., 2024 further show that the method for bridging an observational gap produces errors roughly four times larger than when successive missions overlap.

These projections highlight the urgency for next-generation ERB instruments and complementary observing strategies that are backward compatible, accurate, stable over time, and more cost effective than current designs. Without such innovations, gaps in the ERB record become increasingly likely, threatening the continuity required for reliable Climate Data Records (CDRs). Increasing overlap between successive missions and exploring complementary observing platforms, including emerging CubeSat platforms for ERB, offers practical strategies to mitigate these risks, providing redundancy, flexible launch opportunities, and enhanced intercalibration with larger missions (Gristey et al., 2017; Harber et al., 2019; Swartz et al., 2019).

This paper introduces one promising application to support continuity in the future ERB record by using Earth-viewing measurements from solar irradiance sensors, as demonstrated by the Compact Total Irradiance Monitor (CTIM). CTIM was a 6U CubeSat built at the Laboratory for Atmospheric and Space Physics (LASP) and developed under the NASA In-Space Validation of Earth Science Technologies (InVEST) program to measure total solar irradiance (TSI). CTIM was launched July 2022, collecting climate-quality solar irradiance data at an uncertainty of 0.017% until end-of-mission in December 2023 (Flynn et al., 2024). During orbital eclipse (i.e., Earth nighttime), CTIM was pointed in the nadir direction to opportunistically measure Earth's outgoing longwave radiation. We leveraged this unique opportunity to evaluate the eclipsed CTIM data against coincident CERES data.

This paper compares CTIM outgoing longwave radiance measured during orbital eclipse with coincident CERES observations to determine and utilize opportunistic CTIM Earth-observing applications for complementing NASA's future ERB missions. In doing so, we suggest that future implementations of this type can bridge gaps in ERB observations from space, extending and enhancing CDRs with additional ERB systems that will deepen the understanding of the causes of climate change and predict future climate change more accurately. Section 2 provides an overview of the CERES and CTIM instruments. Section 3 introduces the preliminary analyses of CTIM longwave radiance observations that established the foundation for comparative analysis with CERES. Section 4 details the algorithm created to spatiotemporally match CTIM and CERES observations. Section 5 presents the adjustment factors created to reduce the spread in differences that resulted from viewing geometry differences. Section 6 provides results of the longwave radiance comparisons. Section 7 synthesizes the overall results of the study and discusses the future of complementary CubeSat observations for ERB record continuity.

https://doi.org/10.5194/egusphere-2026-2197
Preprint. Discussion started: 23 April 2026
© Author(s) 2026. CC BY 4.0 License.

2 Instrument Background

2.1 Clouds and Earth's Radiant Energy System (CERES)

Since 2000, the CERES instruments onboard the Terra, Aqua, S-NPP, and NOAA-20 satellites have provided the most spatially and temporally complete record of global shortwave and longwave top-of-atmosphere (TOA) radiative fluxes (Taylor et al., 2022). Each CERES instrument is a narrow field-of-view (NFOV) scanning broadband radiometer, which uses thermistor bolometers to acquire radiometric measurements (Wielicki et al., 1996). CERES instruments aboard Terra, Aqua, and S-NPP measure broadband radiances at the TOA in three spectral regions: shortwave (0.3-5 μm), total (0.3-200 μm), and window (8-12 μm); broadband longwave radiation is estimated as the total minus the shortwave. The CERES instrument FM-6 aboard NOAA-20 replaced the window channel with a longwave channel (Loeb et al., 2018a).

The CERES broadband radiances are converted to irradiances using scene-dependent inversion algorithms based on angular distribution models (ADMs). Before inversion, the radiances are spectrally "unfiltered" to remove the effects of the instrument's spectral response function (Loeb et al., 2001). The resulting irradiances provide a benchmark for quantifying the ERB and for constraining climate model simulations.

2.2 Compact Total Irradiance Monitor (CTIM)

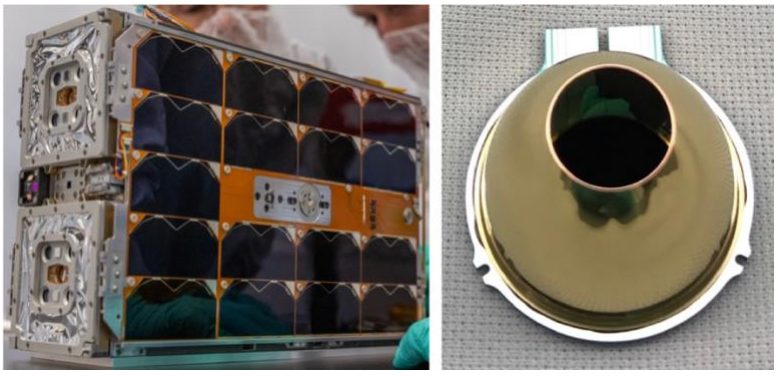

Figure 1: The Compact Total Irradiance Monitor prior to launch vehicle integration (left) and the detector (right).

On 2 July 2022, CTIM was launched into a 500 km altitude, 45º inclination orbit with a 1-year mission goal to demonstrate next-generation technology for monitoring TSI. It returned science data beyond its mission lifetime goal until re-entry in early December 2023 (Flynn et al., 2024). CTIM used electrical substitution radiometers (ESRs) with a vertically aligned carbon nanotube (VACNT) absorber with a thermally integrated reflective dome. CTIM accommodated two independent detector heads, each with four TSI channels. One primary channel on each of the detector heads received maximum solar exposure, while the remaining three were operated at varying cadences to track the detector degradation to maintain stability over time. The CTIM VACNT detectors are nearly ideal optical absorbers over a very broad spectral range (Harber et al., 2019; Tomlin et al., 2020). As a next-generation technology demonstration for TSI, CTIM successfully measured TSI within

https://doi.org/10.5194/egusphere-2026-2197
Preprint. Discussion started: 23 April 2026
© Author(s) 2026. CC BY 4.0 License.

0.04% of the Total Irradiance Monitor (TIM) measurements from the Total and Spectral Solar Irradiance Sensor (TSIS-1) mission, shown in Fig. 2. In addition, CTIM demonstrated measurements of TSI with long-term stability comparable to that of TSIS-1 TIM (Coddington et al., 2025). Beyond the primary mission to measure TSI, the CTIM Earth-viewing observations provided ample data to explore its observational capabilities of Earth's outgoing radiation.

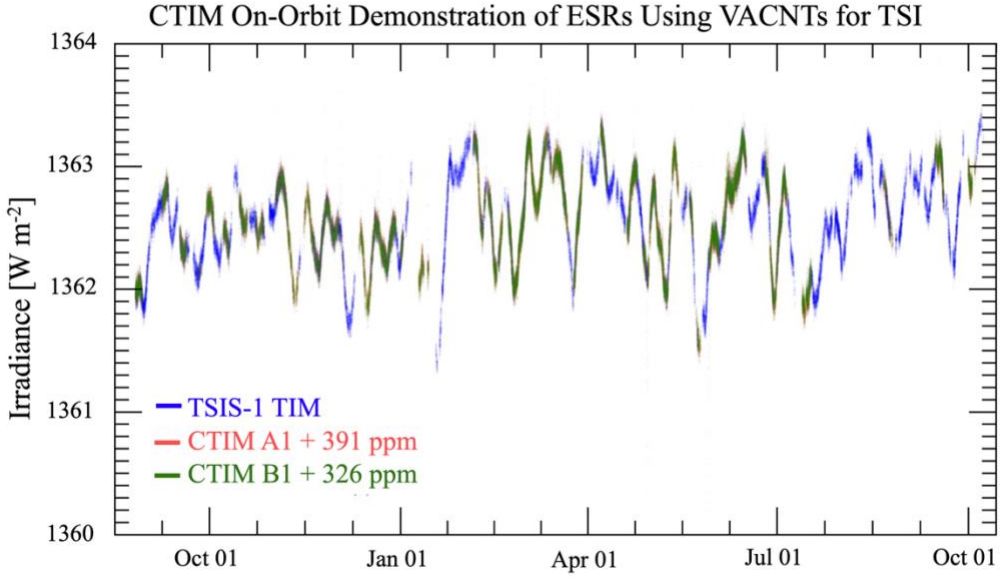

Figure 2: CTIM measured TSI from dual detector heads, A1 and B2, compared to the TSI measured by TSIS-1 TIM.

3 CTIM Earth-Viewing Observations

CTIM observed deep space every other eclipse to establish the instrument dark model (Harber et al., 2019). During the other eclipse periods, the instrument was pointed at Earth nadir, collecting 28,321 observations of the outgoing terrestrial longwave radiance from 26 August 2022 through November 18, 2023. CTIM continued to acquire TSI measurements during the remainder of the orbit, while occasionally observing the sunlit Earth a total of 4,633 times between August 27, 2022, and August 24, 2023. Using this data, we converted the CTIM calibrated irradiance to radiance (Sect. 3.1), separated the day and night observations (Sect. 3.2), and conducted preliminary longwave radiance analyses (Sect. 3.3), which became the groundwork for comparative analysis with CERES observations in this study.

https://doi.org/10.5194/egusphere-2026-2197
Preprint. Discussion started: 23 April 2026
© Author(s) 2026. CC BY 4.0 License.

3.1 CTIM Irradiance-to-Radiance Conversion

Because CTIM was designed to measure TSI, it was calibrated in irradiance, requiring a conversion to radiance to compare to the CERES direct measurement. The relationship between CTIM irradiance, *F,* and radiance, *L*, over the CTIM angular field-of-view (FOV) is given by:

$$F = \int_0^{2\pi} \int_0^{\frac{\pi}{2}} L(\theta,\varphi) r(\theta,\varphi) \sin\theta \, d\theta d\varphi \quad (1)$$

where $L(\theta,\varphi)$ is the directionally dependent radiance within the CTIM view, $r(\theta,\varphi)$ is the normalized CTIM angular response with respect to normal, and θ and φ are polar and azimuth angle, respectively.

Since *r* was azimuthally symmetric, we can rewrite Eq. (1):

$$F = \bar{L}\Omega_e \quad (2)$$

where,

$$\bar{L} = \frac{\int_0^{2\pi} \int_0^{\frac{\pi}{2}} L(\theta,\varphi) r(\theta) \sin\theta \, d\theta d\varphi}{2\pi \int_0^{\frac{\pi}{2}} r(\theta) \sin\theta \, d\theta} \quad (3)$$

and *effective* solid angle, Ω_e, is

$$\Omega_e = 2\pi \int_0^{\frac{\pi}{2}} r(\theta) \sin\theta \, d\theta \quad (4)$$

Based on measurements conducted in lab, the CTIM off-normal angular response (Fig. 3) reached zero at 23°. Numerical integration of Eq. (4) resulted in an effective CTIM solid angle of 0.0939 sr; substitution in Eq. (2) was used to compute mean radiance from the measured irradiance.

https://doi.org/10.5194/egusphere-2026-2197
Preprint. Discussion started: 23 April 2026
© Author(s) 2026. CC BY 4.0 License.

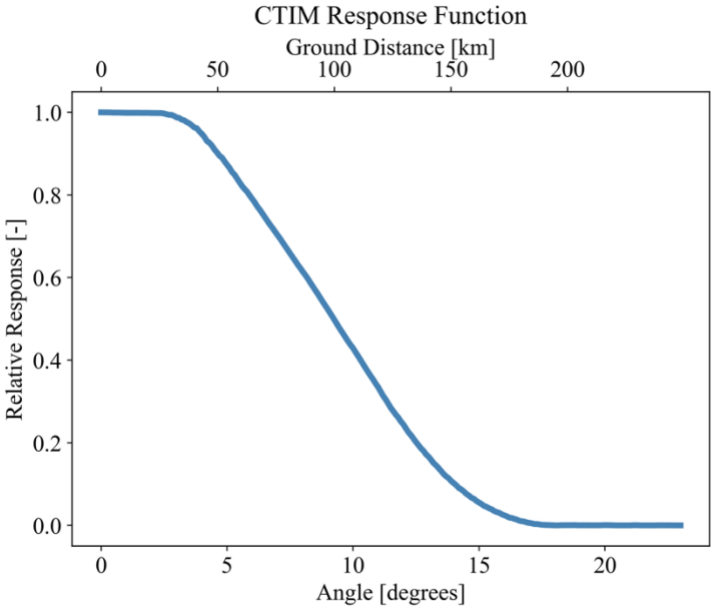

Figure 3: CTIM angular response function. The bottom x-axis shows the angle of incidence of incoming radiation; the top x-axis shows the equivalent ground distance from nadir. The y-axis shows the detector's normalized response.

3.2 Separation of Day and Night Observations

From August 2022 to November 2023, CTIM collected 32,954 observations of Earth. Of the two CTIM detector heads, A1 and B1, only observations from A1 were used in this analysis, since Earth radiance observational differences between the detectors were generally less than 0.3%. The Earth-viewing observations were then separated into daytime and nighttime using the CTIM Sun-satellite angle and Fine Sun Sensor (FSS) data values. The CTIM Sun-satellite angle was measured between CTIM and the Sun when CTIM was pointed at Earth nadir, separate from TSI observation periods. Because Earth eclipsed the CTIM view of the Sun, the angle for nighttime observations was acute compared to daytime observations. The FSS was the reading from the fine sun sensor quadrant photodiodes. During eclipse, the FSS values were naturally very low. By examining the FSS readout as a function of the Sun-satellite angle, we determined the Sun-satellite angle cutoff between night and day observations. Figure 4 shows a steep incline in CTIM FSS reading just above a CTIM Sun-satellite angle of 80°. This abrupt increase in signal represented the transition to daytime observations, so we used a Sun-satellite angle cutoff of 80° to separate eclipsed observations for longwave radiation analysis. This process resulted in 28,321 CTIM observations of Earth during orbital eclipse.

Figure 5 shows all the CTIM Earth observations, as well as the separated day and night observations resulting from the filtering process shown in Fig. 4. Daytime observations reached higher radiance values than nighttime observations, but nighttime observations occurred more frequently and dominated the CTIM Earth-viewing dataset. Since the CTIM primary

https://doi.org/10.5194/egusphere-2026-2197
Preprint. Discussion started: 23 April 2026
© Author(s) 2026. CC BY 4.0 License.

mission was to measure TSI, the number of times it was pointed to Earth during the daytime was far less compared to observations during eclipse.

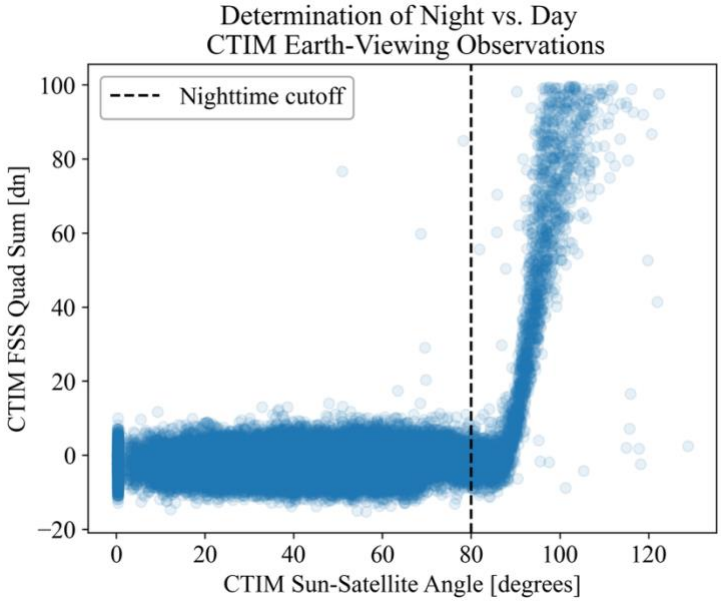

Figure 4: Determination of CTIM Earth-eclipsed observations from the CTIM FSS Quad Sum and CTIM Sun-Satellite Angle. Datapoints accepted as eclipsed data had a Sun-satellite angle less than 80°.

https://doi.org/10.5194/egusphere-2026-2197
Preprint. Discussion started: 23 April 2026
© Author(s) 2026. CC BY 4.0 License.

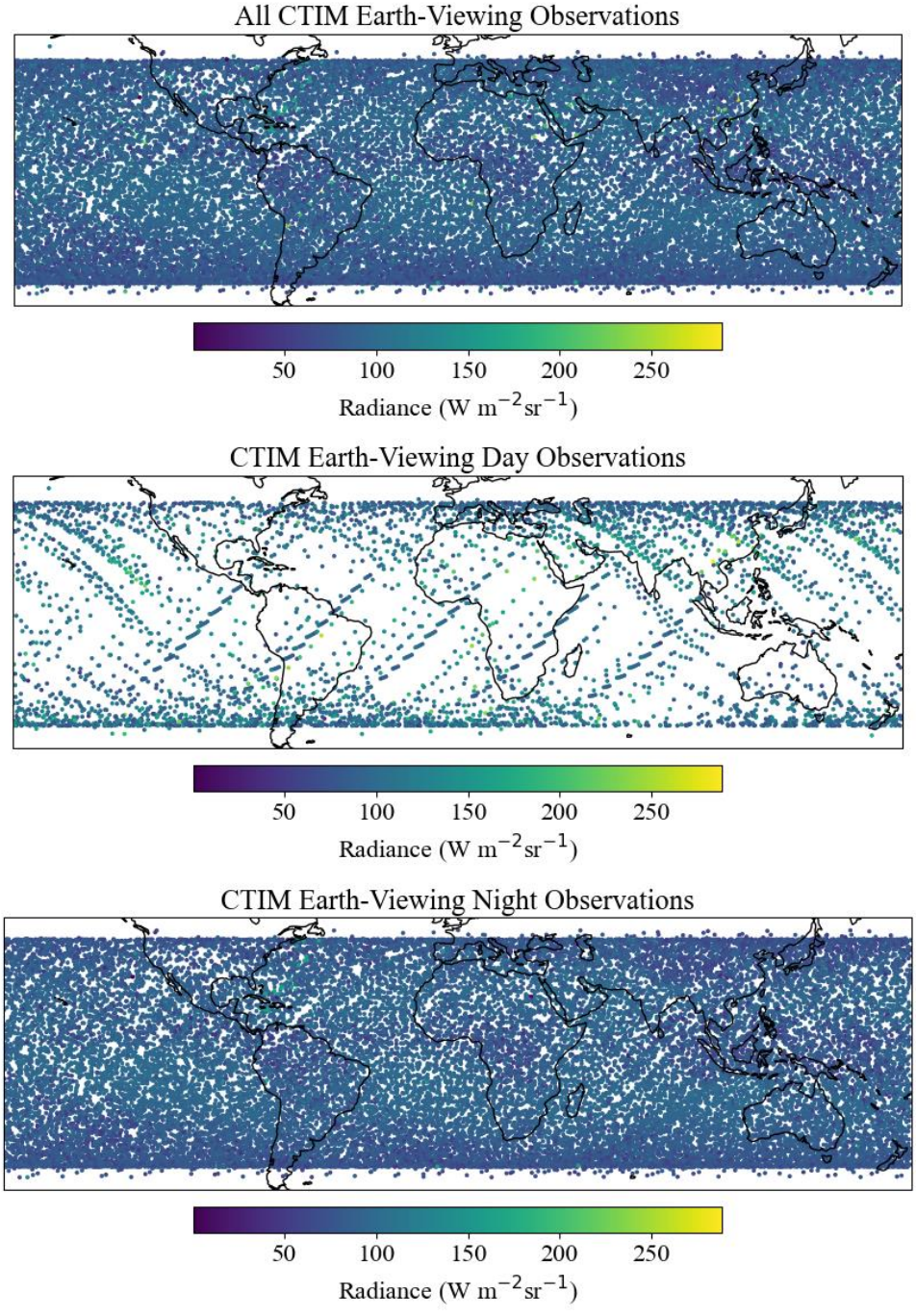

Figure 5: Global coverage of CTIM Earth-viewing observations. Top: All CTIM Earth-viewing observations including both daytime and nighttime observations. The separated day (middle) and night (bottom) observations resulted from the process shown in Fig. 4.

https://doi.org/10.5194/egusphere-2026-2197
Preprint. Discussion started: 23 April 2026
© Author(s) 2026. CC BY 4.0 License.

3.3 Evaluation of CTIM Longwave Radiance Observations

The latitudinal variation of outgoing longwave radiation, known since the earliest ERB measurements from space (Vonder Haar & Suomi, 1971), was exhibited in CTIM data collected during orbital eclipse (Fig. 6). When averaged per degree of latitude, the CTIM radiances showed a local minimum over the tropics, indicating strong convective cloud cover in the inter-tropical convergence zone (ITCZ).

The spatially gridded variation of 15 months of CTIM longwave radiance data is shown in Fig. 7 and was qualitatively compared to 17 years of CERES data. Areas of local maxima and minima matched to similar features in the CERES average global outgoing longwave irradiance. Specifically, the highlighted areas of low radiative energy emission in equatorial regions in Fig. 7 aligned with the equatorial local minima in Fig. 6, both representative of high, cold clouds in the ITCZ.

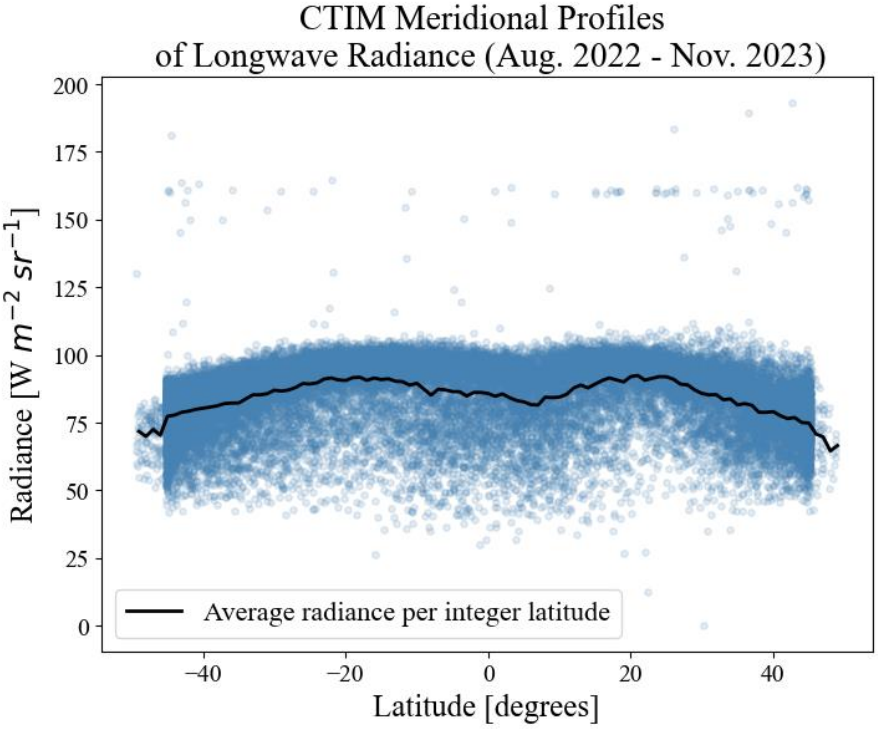

Figure 6: CTIM longwave radiance variation by latitude. Blue points represent individual CTIM radiances, and the black line represents the average radiance per degree latitude.

https://doi.org/10.5194/egusphere-2026-2197
Preprint. Discussion started: 23 April 2026
© Author(s) 2026. CC BY 4.0 License.

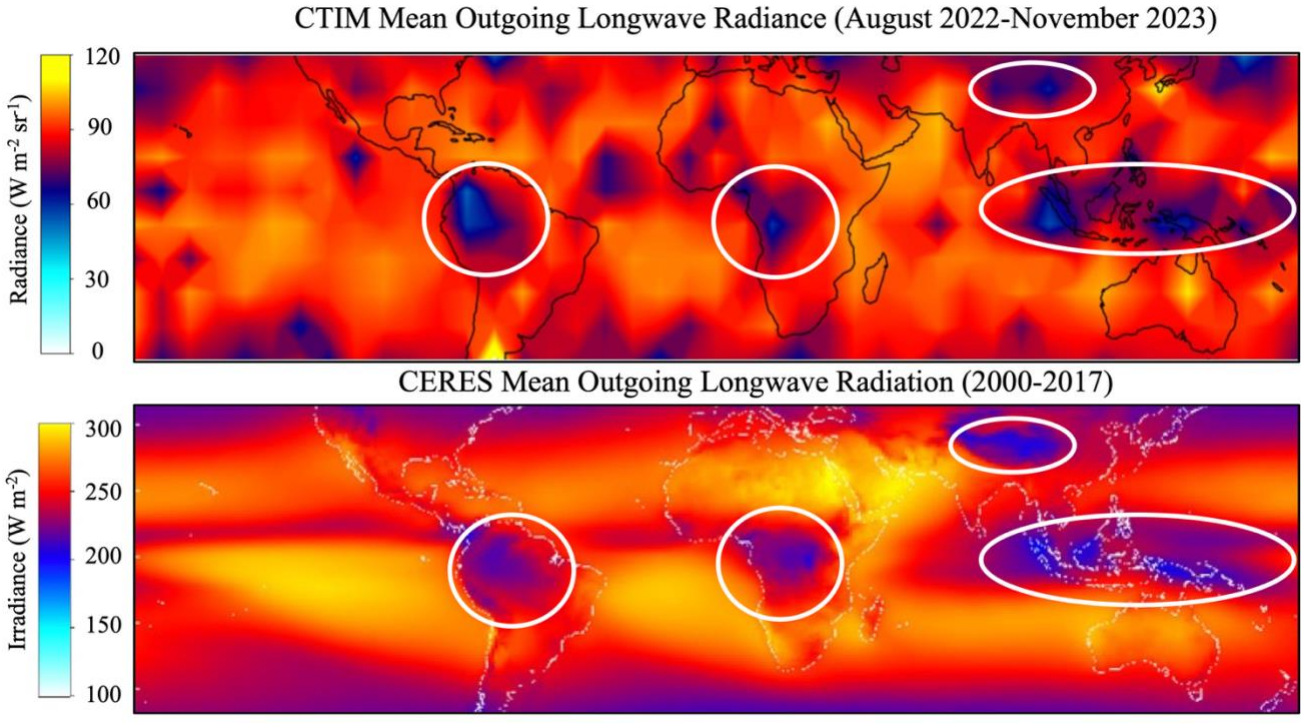

Figure 7: Global longwave radiation. Top: All CTIM longwave radiance from the A1 detector spatially gridded at ~4º resolution for 15 months of observations. All observed radiances within an approximate 4º bin were bin-averaged to determine the pixel radiance within the CTIM latitude range. Bottom: CERES all-sky outgoing longwave radiation averaged over seventeen years of observations from Terra and Aqua (adapted from Dewitte & Clerbaux, 2018). Yellow-red regions represent areas of high longwave radiation emission, and purple-blue regions represent areas of low longwave radiation emission. Note the CERES radiative energy is expressed in irradiance (W/m^2), and the CTIM radiative energy is expressed in radiance (W/m^2 sr). Despite the different units, localized concentrations of radiative energy are qualitatively similar, specifically low areas of radiative energy that are highlighted by the white circles.

4 Matching Algorithm for CTIM and CERES

To conduct our comparative analysis between CTIM and CERES, we developed a four-step algorithm for matching the instruments' ground-projected footprints space and time. CERES FM-1 and FM-2 on Terra, FM-3 and FM-4 on Aqua, and FM-6 on NOAA-20 were selected for comparison, while FM-5 on S-NPP was excluded as it was primarily operating in rotating azimuth plane scan (RAPS) mode during the CTIM lifetime. In RAPS mode, CERES scans in elevation while the scan plane continuously rotates around the satellite nadir axis, producing footprints with varying view zenith angles and continuously changing azimuth relative to the surface, resulting in far fewer collocations with nadir-viewing or cross-track

https://doi.org/10.5194/egusphere-2026-2197
Preprint. Discussion started: 23 April 2026
© Author(s) 2026. CC BY 4.0 License.

instruments. For the CERES instruments aboard Terra, Aqua, and NOAA-20, we used CERES Single Scanning Footprint-Level 2 (SSF) Edition4A data products, which provide TOA shortwave and longwave radiances (Loeb et al., 2016).

There were fundamental differences in how CTIM and CERES viewed the Earth. CTIM acquired nadir observations with a line of sight perpendicular to Earth's surface with a footprint approximately 200 km in diameter. In contrast, the CERES instruments operated in cross-track scanning mode, sweeping from limb to limb, perpendicular to the satellite ground track. The CERES viewing zenith angles (VZAs) reached extrema of ~66° for Terra and Aqua, and ~71° for NOAA-20 (Su et al., 2020). Because CERES scans in a continuous sweep, the VZA varies for each footprint. The CERES footprint diameter is approximately 20 km at nadir for Terra and Aqua, and 24 km for NOAA-20 (Loeb et al., 2018b). Given the substantially larger CTIM footprint, each CTIM observation was populated with many CERES footprints. An algorithm was developed to spatiotemporally collocate CTIM and CERES observations.

Step 1. CERES footprints were selected based on spatial and temporal proximity to CTIM footprints within pre-defined parameters. The CTIM dataset included latitude, longitude, time, and radiance for each footprint. CERES SSF Level-2 data were preprocessed to retain only those footprints with a VZA of 20°or less, ensuring observations were near-nadir, within the range of CTIM angular response and thus, more directly comparable to the CTIM nadir observations. Using these CERES data, we applied a temporal constraint of ±20 minutes relative to each CTIM footprint timestamp to avoid sampling across multiple CERES orbits. The Aqua and Terra orbital periods are approximately 99 minutes, and that of NOAA-20 is approximately 101 minutes (Parkinson et al., 2006; *JPSS Performance Status*, 2025). Given the CTIM footprint radius of ~100 km, as determined by the CTIM angular response function (Fig. 3), a spatial constraint of 100 km from the CTIM centroid was applied to maximize CERES coverage within each footprint. We determined that a minimum threshold of 75 CERES samples within the CTIM footprint that met the time and VZA criteria was sufficient to optimize three objectives: maintain near-nadir observations for direct comparison with CTIM; ensure near-full CERES coverage over each CTIM footprint; and maximize the total number of CTIM–CERES matches. Each resulting CTIM–CERES "match" therefore consisted of at least 75 CERES footprints collocated within ±20 minutes and within 100 km of the CTIM footprint, each with a VZA of 20° or less.

Step 2. For CTIM–CERES matches from Step 1 where spatial coverage was incomplete (i.e., areas within the CTIM footprint not sampled by footprints with VZA of 20° or less), additional CERES observations at any VZA within the same spatiotemporal constraints (±20 minutes, 100 km radius) were included to fill these gaps. Although these supplemental CERES footprints could come from all VZAs (that could be as large as 71º), the geometry of CERES cross-track scanning naturally limited the maximum VZA to 23.14° within the 100-km radius around each CTIM centroid. As shown in Fig. 8, only 0.5% of all CERES observations in the dataset resulting from Steps 1 and 2 (approximately 0.4 supplementary footprints per CTIM–CERES match on average) had VZA greater than 20°. This procedure retained all 722 CTIM–CERES

https://doi.org/10.5194/egusphere-2026-2197
Preprint. Discussion started: 23 April 2026
© Author(s) 2026. CC BY 4.0 License.

matches from Step 1, resulting in a total of 60,739 CERES footprints (average of 84 footprints per match), with the vast majority representing near-nadir observations closely matching CTIM's viewing geometry.

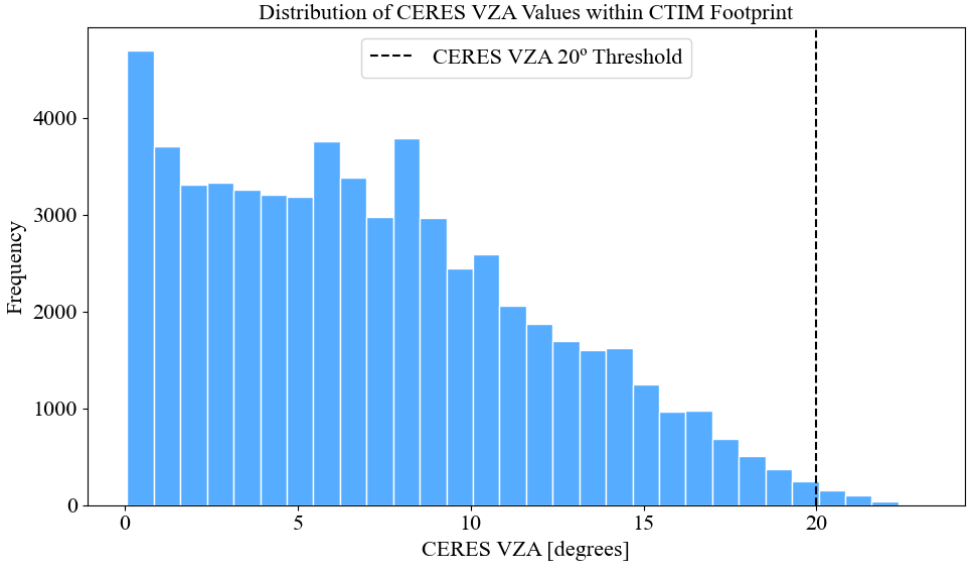

Figure 8: Distribution of CERES VZAs within CTIM footprints. The orange line exhibits the VZA 20º threshold applied in Step 1 of the matching algorithm, showing the 0.5% of CERES footprints with a VZA greater than 20º.

Step 3. CERES radiances were weighted by the CTIM spatial response function, the footprint area ratio as a function of VZA, and limb-darkening adjustment factors for clear-sky scenes (see Sect. 5). The CTIM spatial response function (the distance equivalence to the angular response) is shown in Fig. 3. To weight the CERES radiances with the CTIM spatial response, we first determined the distance each CERES footprint was from the center of the CTIM footprint, as given by each latitude and longitude. The weightings were determined from the distance from CTIM spatial response centroid for all CERES footprint radiances.

Step 4. The mean CERES weighted radiance for each CTIM footprint was determined with the weighted radiances from Step 3, such that each CTIM–CERES match provided a comparison between a mean CERES radiance and a CTIM mean radiance.

https://doi.org/10.5194/egusphere-2026-2197
Preprint. Discussion started: 23 April 2026
© Author(s) 2026. CC BY 4.0 License.

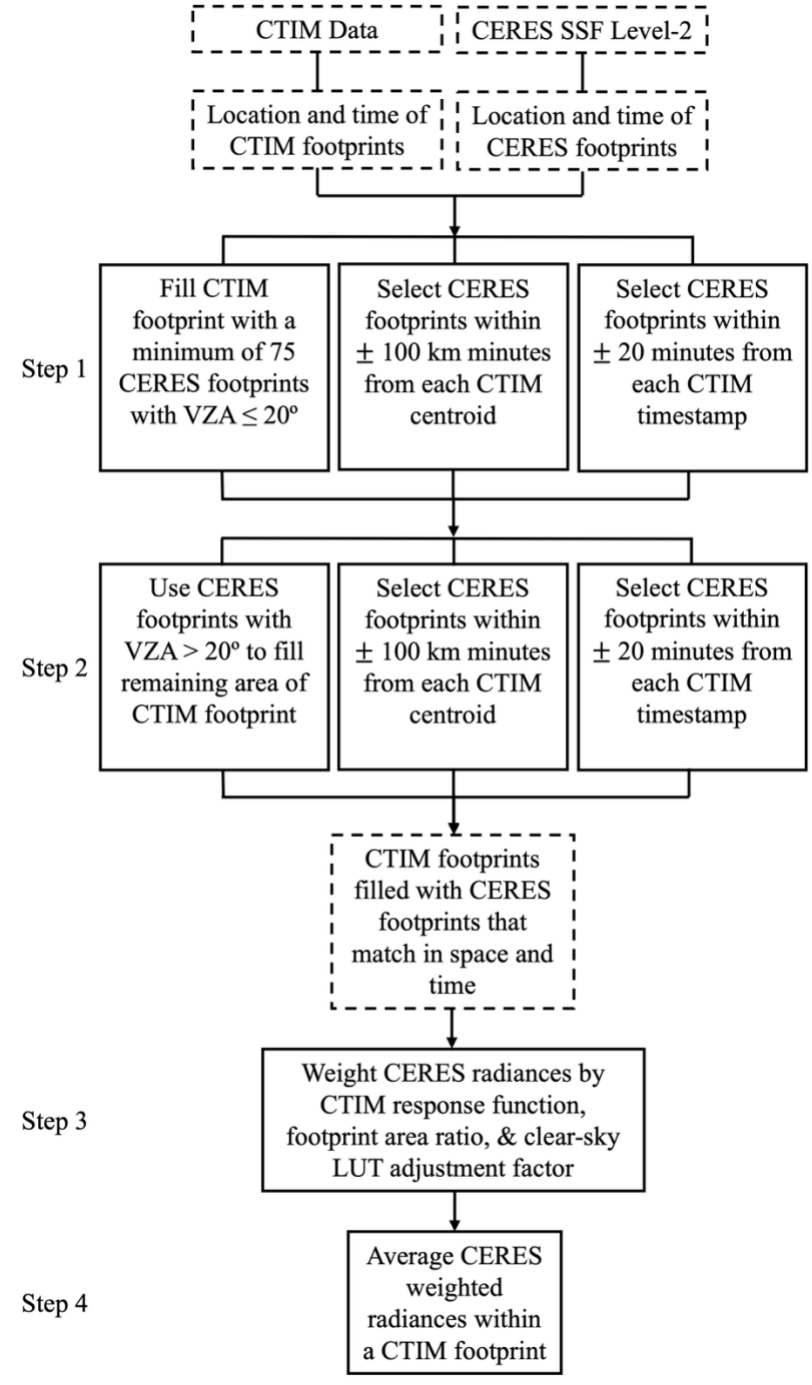

Figure 9: Processing flow for CTIM and CERES matching. Solid boxes were action steps and parameters. Dashed boxes were data inputs (outputs) for (from) steps.

https://doi.org/10.5194/egusphere-2026-2197
Preprint. Discussion started: 23 April 2026
© Author(s) 2026. CC BY 4.0 License.

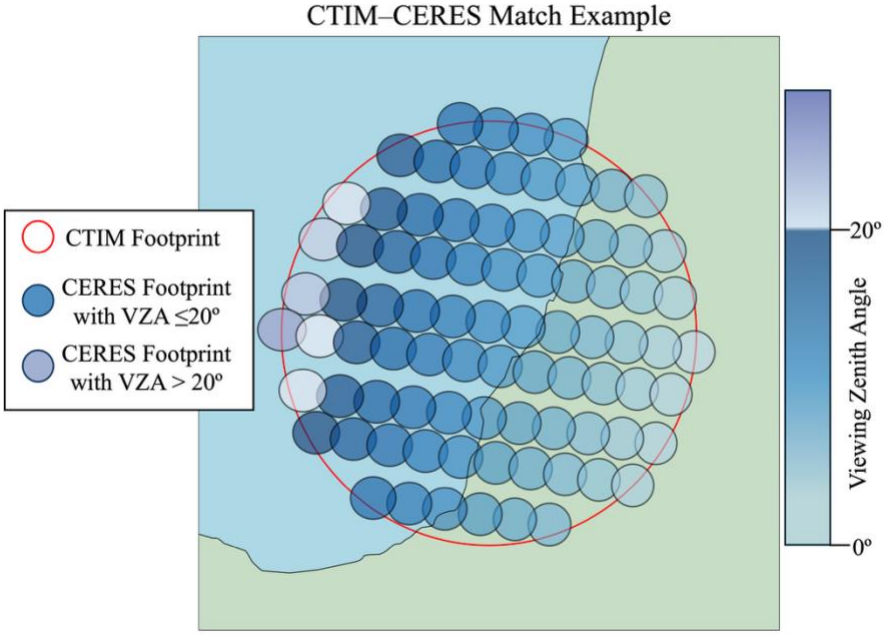

Figure 10: One resulting CTIM–CERES match from the matching algorithm. The CTIM footprint (large red circle) is populated with CERES footprints (small blue- and purple-filled circles and ellipses). Blue-filled CERES footprints represent all CERES footprints with a VZA ≤ 20° (Step 1), where a darkening blue represents a VZA closer to 20°. Purple-filled CERES footprints result from Step 2, where the remaining CTIM area from Step 1 is populated with CERES footprints with a VZA > 20°. Darkening purple represents a VZA increasing above 20°. CERES footprints become increasingly elliptical at larger VZAs, which is accounted for in Sect. 5.2.

5 Adjustments for CERES VZA

5.1 Comparison Before Adjustments for CERES VZA

In initial comparisons, the algorithm outlined in Sect. 4 did not include adjustments for CERES viewing geometry. Before accounting for the CERES viewing geometry and only weighting the CERES radiances by the CTIM response function, the agreement between CTIM and CERES radiances was within 1.29% but with spread about the mean (standard deviation, σ, of the relative differences was 4.23%) (Fig. 11). While the negative bias is small between the two instruments, we focused on reducing the spread in the statistical comparison. We hypothesized the spread was due, in part, to the different viewing geometries between CTIM and CERES. From this hypothesis, we first adjusted the CERES footprint area as a function of VZA (Sect. 5.2). In an effort to reduce the spread further, we considered adjusting CERES radiances due to limb darkening for off-nadir radiance. Therefore, we conducted radiative transfer simulations to examine limb-darkening effects of non-nadir viewing for CERES radiances to assess potential viewing geometry impacts on the comparison of radiances (Sect. 5.3-5.5).

https://doi.org/10.5194/egusphere-2026-2197
Preprint. Discussion started: 23 April 2026
© Author(s) 2026. CC BY 4.0 License.

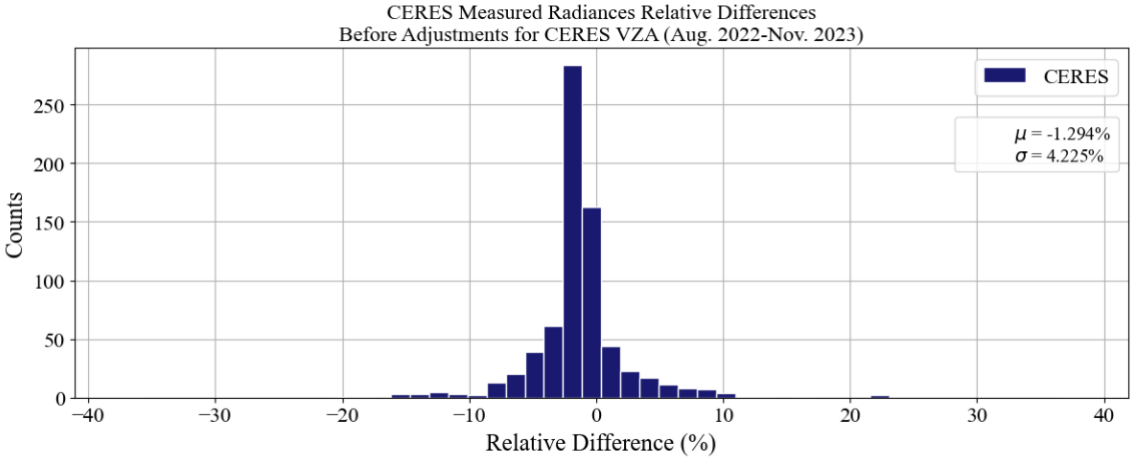

Figure 11: Distribution of relative differences (see Eq. (6)) between CTIM and CERES before applying adjustments for CERES VZA. CERES radiances were only weighted by the CTIM response function.

5.2 VZA Influence on CERES Footprint Areas

Since CERES scans Earth in cross-track mode, the CERES pixel footprint projected at Earth's surface grows with increasing VZA (as illustrated in Fig. 10). The CERES footprint at nadir was approximated as a circular field of view (FOV) with a diameter of 20 km for Terra and Aqua and 24 km for NOAA-20. Although the instrument's physical field stop is hexagonal, the point spread function and optical blur produce an approximately elliptical footprint commonly represented as a circular "equivalent" at nadir, encompassing ~95% of the PSF response (Green & Wielicki, 1997). As the cross-track scanner moves from nadir, the footprint semi-major axis increases with the slant range, and the footprint becomes elliptical. Due to Earth's rotation, the center points of the large VZA are displaced from the ground track. Smith et al. (1994) warrant no concern for such small displacements. Appropriate weighting was applied to account for biases that could arise from the variable footprint area for each CERES footprint off nadir.

The CERES VZA at the sensor (θ') was determined from the CERES VZA at the surface (θ) given by the SSF Level-2 data, following methods adapted from Jahani et al. (2022). The Earth was assumed to be spherical, and the law of sines was applied as shown in Fig. 12. Once θ' was determined, the cross-scan length of the CERES footprint ($l_{cross\text{-}scan}$; km) was approximated by first assuming the Earth to be flat on the CERES footprint scale and second, assuming the semi-major axis of the ellipse to be the average of l_1 and l_2. The along-scan length was assumed to be constant at either 20 km for Terra and Aqua or 24 km for NOAA-20. Using the cross-scan and along-scan lengths, the CERES footprint areas were computed as a function of VZA. A footprint area ratio was determined by dividing the footprint area off nadir by the footprint area at nadir

https://doi.org/10.5194/egusphere-2026-2197
Preprint. Discussion started: 23 April 2026
© Author(s) 2026. CC BY 4.0 License.

for all VZAs. The footprint area ratio for each satellite was used in the weighting process (Sect. 4, Step 3) to determine the mean CERES radiance in each CTIM footprint (Sect. 4, Step 4).

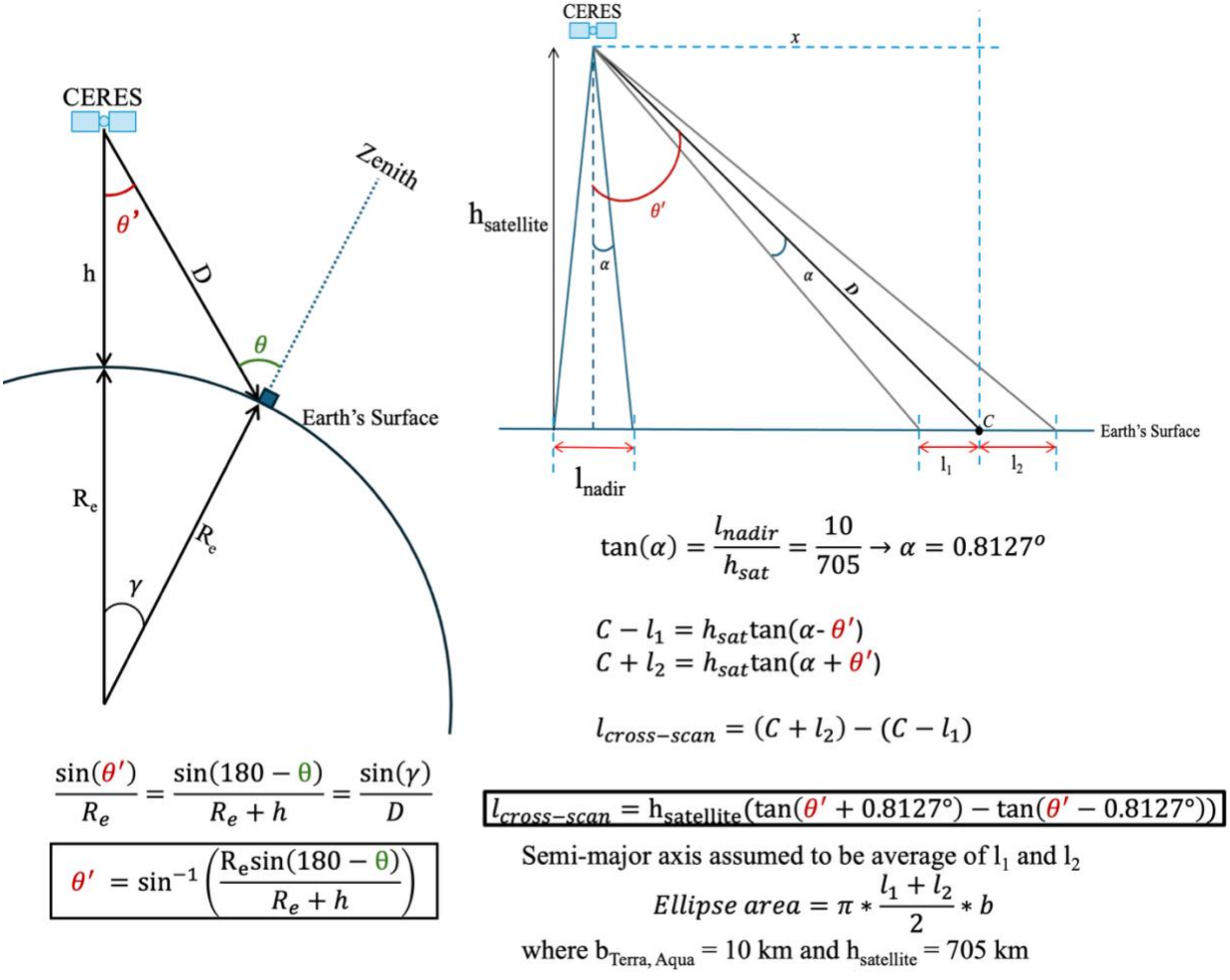

Figure 12: Geometry for determining the CERES footprint area as VZA increased off nadir (adapted from Jahani et al., 2022). Left: Law of sines determined the VZA at the CERES sensor (θ'), given the CERES VZA at the surface (θ). Right: Determination of the cross-scan width for Terra and Aqua as the VZA at the CERES sensor increased.

5.3 VZA Influence on Limb Darkening

The radiance exiting at the TOA typically decreases in magnitude with increasing angle from nadir due to the increase in path length and the decrease in temperature with altitude. So-called *limb-darkening* models describe the variations in radiance with viewing angle (Smith et al., 1994). The MODerate spectral resolution TRANsmittance (MODTRAN) radiative

https://doi.org/10.5194/egusphere-2026-2197
Preprint. Discussion started: 23 April 2026
© Author(s) 2026. CC BY 4.0 License.

transfer code was used to create lookup tables (LUTs) to derive limb-darkening corrections to apply to CERES off-nadir radiances as a function of scene type and atmospheric composition for clear-sky scenes.

To date, only a clear-sky adjustment has been developed, as limb-darkening effects from clouds may be larger: at larger viewing angles, radiation traverses longer paths through cloud layers, encountering more absorption and greater contribution from emission by cooler cloud tops and edges (Clerbaux et al., 2020; Loeb et al., 2005). The path through the clouds at oblique viewing angles reduces the radiance relative to nadir more than in clear-sky conditions, where emission is dominated by the surface and lower troposphere. In addition, each CERES SSF Level-2 footprint includes multiple interacting cloud properties—such as cloud fraction, cloud optical depth, cloud top height, and vertical layer structure—that collectively modulate outgoing longwave radiance at different viewing angles. Accounting for all of these interactions substantially increases the complexity of radiative transfer calculations for limb-darkening corrections for each CERES footprint, beyond the scope of the present study.

MODTRAN provides accurate and rapid simulations, computing line-of-sight atmospheric spectral transmittances and radiances for stratified, horizontally homogeneous atmospheres from the ultraviolet through the far-infrared spectrum (Berk et al., 2014). Because MODTRAN solves the radiative transfer equation along any line of sight, it was used to determine radiance changes with viewing angle for constructing limb-darkening adjustments for clear-sky scenes. The goal of these adjustments was to minimize the spread in the difference between CTIM and CERES radiances (Fig. 11), which we hypothesized might depend, in part, on the mismatches in VZA between CTIM and CERES.

5.4 Parameters for MODTRAN Simulations

To employ MODTRAN for clear-sky limb-darkening corrections, we varied four parameters: VZA, surface emissivity, surface temperature, and atmosphere model. Each CERES footprint included the SSF Level-2 data for surface emissivity, surface temperature, and VZA; the standard MODTRAN model atmospheres were determined by footprint latitude and date. This section details the selected parameters.

To determine the variations in radiance with viewing angle for the LUTs, the VZA distribution amongst all CERES footprints within our CTIM–CERES matches was used for determining the range of VZAs for MODTRAN simulations. While we constrained the CERES footprint criteria to 75 footprints with a VZA of 20º in our matching algorithm to best match CTIM nadir viewing, 0.5% of CERES footprints had a VZA greater than 20º with a maximum VZA of 23.14º (Fig. 8). From the CERES VZA distribution, we selected four VZAs for the MODTRAN simulations: 0º, 8º, 17º, and 25º.

https://doi.org/10.5194/egusphere-2026-2197
Preprint. Discussion started: 23 April 2026
© Author(s) 2026. CC BY 4.0 License.

Surface emissivity and surface temperature determine the amount of radiation leaving the surface. Each surface type on Earth has a distinct emissivity. CERES uses the International Geosphere-Biosphere Programme (IGBP) surface type classification to determine surface broadband emissivity. The IGBP defines 18 distinct surface types (e.g., mixed forest, evergreen needleleaf, etc.) as a comprehensive system for organizing different Earth surface types for studying global environmental processes. For each CERES footprint, an IGBP surface type is determined in the SSF Level-2 data. From the 18 IGBP surface types, each surface type broadband emissivity ranges approximately between 0.890-1.0 (CERES Surface Type IDs, 2025). Emissivity values, ε, were selected within this range to represent surface types in the MODTRAN simulations. In MODTRAN, the surface type was simulated by inputting the albedo (1- ε) for a Lambertian surface. A wavelength range of 0.3-300 μm was selected with a user-defined albedo (USDALB) = 1- ε for all ε: 0.89, 0.91, 0.93, 0.95, 0.97, 0.99, 1.00. We used a range of surface temperatures from 260 K to 310 K for each of the six surface emissivities.

MODTRAN provides six atmosphere base profiles of temperature, pressure, and molecular and aerosol composition. The three relevant atmosphere models applied in this study were tropical, mid-latitude summer, and mid-latitude winter, since CTIM covered approximately 40° N to 40° S. The MODTRAN tropical model simulates a tropical atmosphere between 15° latitude; the mid-latitude summer and winter atmosphere models are between 15°- 45° N and S latitude.

Using these parameters (listed in Table 1), 504 MODTRAN simulations were conducted to generate limb-darkening adjustment factors for clear-sky CERES radiances. An adjustment factor was calculated as in Eq. (5) for all simulated radiances. For example, the 8° VZA, 0.89 surface emissivity, 260 K surface temperature, mid-latitude summer atmosphere model radiance was compared to the 0° VZA, 0.89 surface emissivity, 260 K surface temperature, mid-latitude summer atmosphere model radiance to find the 8° VZA radiance relative difference to the 0° VZA.

MODTRAN Parameters for Simulating CERES Longwave Radiance Observations			
VZA (°)	**Surface Emissivity**	**Surface Temperature (K)**	**Atmosphere Model**
0	0.89	260	Tropical
8	0.91	270	Mid-latitude Summer
17	0.93	280	Mid-latitude Winter
25	0.95	290	
	0.97	300	
	0.99	310	
	1.00		

Table 1: MODTRAN parameters used for simulating CERES longwave radiance observations.

https://doi.org/10.5194/egusphere-2026-2197
Preprint. Discussion started: 23 April 2026
© Author(s) 2026. CC BY 4.0 License.

$$Adjustment\ Factor = \frac{Radiance_{nadir}}{Radiance_{off\ nadir}} \quad (5)$$

The results of the mid-latitude summer atmosphere model simulation are shown in Fig. 13. As the VZA increased off nadir, the adjustment factor increased. Similarly, as surface temperature and surface emissivity increased, the adjustment factor increased. While the adjustment factor values changed slightly for each atmosphere model with the given variables, the trend remained the same for all three atmosphere models: As surface temperature increased, emissivity increased, and VZA increased, the simulated radiance decreased compared to the radiance at nadir. While the adjustment factors were small in magnitude, we applied them to clear-sky scenes to ensure that CERES off-nadir radiances were consistent with CTIM nadir-viewing geometry, thereby enabling a more direct comparison between the datasets.

https://doi.org/10.5194/egusphere-2026-2197
Preprint. Discussion started: 23 April 2026
© Author(s) 2026. CC BY 4.0 License.

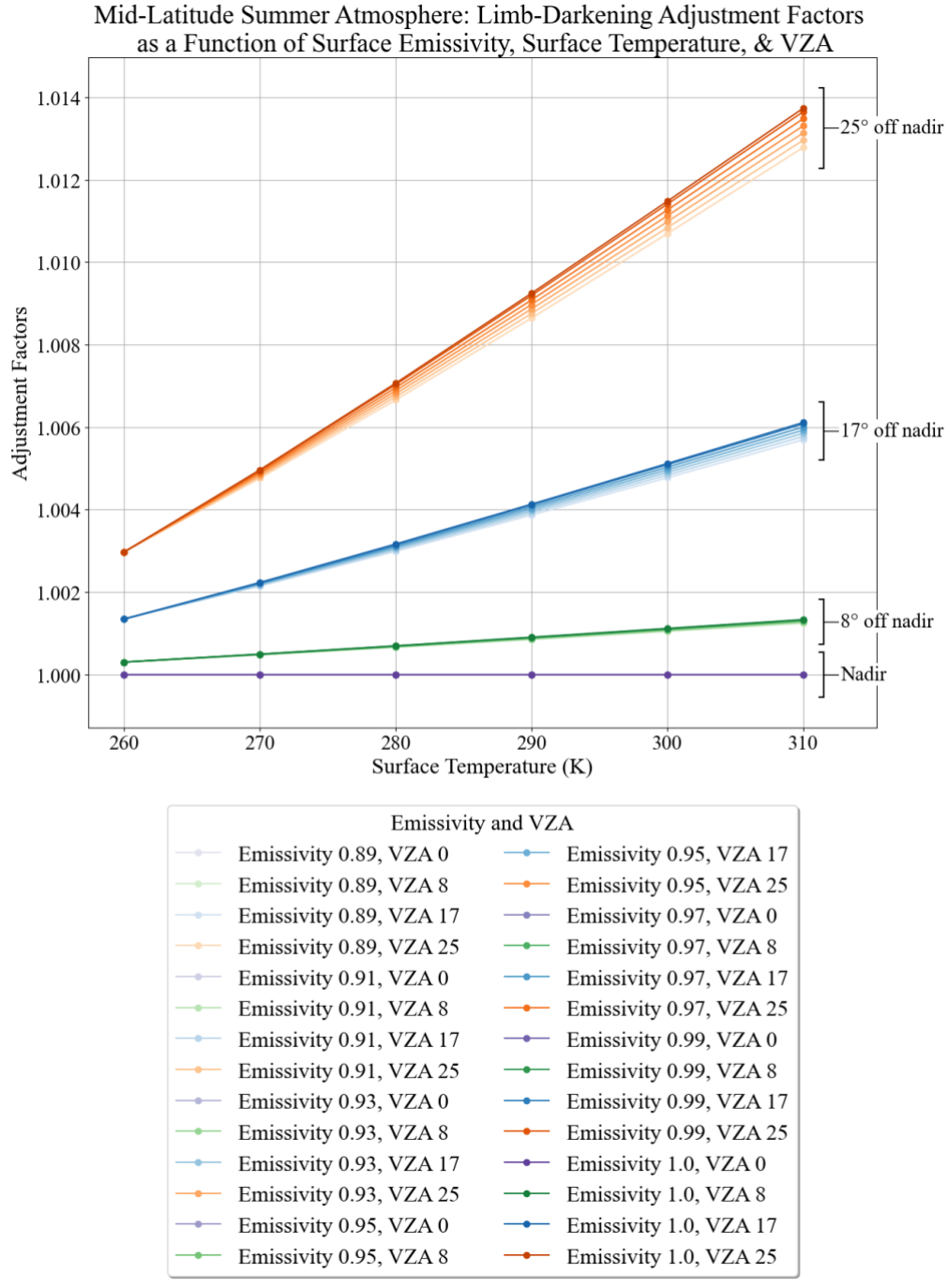

Figure 13: Limb-darkening effects based on surface temperature, emissivity, and degrees off nadir for a mid-latitude summer atmosphere. Each color represents a different value of VZA. Darkening color represents higher emissivity. The highest adjustment factor resulted from 25° off nadir, 1.0 emissivity, and 310 K surface temperature.

https://doi.org/10.5194/egusphere-2026-2197
Preprint. Discussion started: 23 April 2026
© Author(s) 2026. CC BY 4.0 License.

5.5 MODTRAN-Derived Limb-Darkening Corrections

To apply the clear-sky LUT adjustment factors to CERES-observed radiances, the SSF Level-2 clear-sky fraction data was used to determine clear-sky scenes for any CERES footprint within any CTIM footprint. Any CERES footprint that matched within any of the CTIM footprints with a clear-sky percentage of 95% or greater was defined as a clear-sky scene.

The clear-sky CERES footprints were sorted into hemispheric regions: tropical, Northern Hemisphere, or Southern Hemisphere. Based on the date of observation and hemispheric region, the footprints were further sorted into tropical, summer, or winter seasons. Once sorted by season, each footprint was matched with a MODTRAN atmosphere model. As a result, all clear-sky CERES footprints within the CTIM–CERES matches were mapped onto one LUT adjustment factor value based on atmosphere model, surface emissivity and temperature, and VZA to interpolate an appropriate limb-darkening adjustment factor. The adjusted radiance was calculated by multiplying the observed CERES radiance by the adjustment factor (Eq. (5)) in Step 3 of the matching algorithm described in Sect. 4. By adjusting the CERES radiances for off-nadir viewing, we accounted for limb-darkening effects in clear-sky scenes that influenced the radiance differences between CTIM and CERES.

6 Results

Using the matching algorithm detailed in Sect. 4, we found 722 matches between CTIM and CERES and applied the VZA adjustments discussed in Sect. 5. We grouped CERES instruments by their host satellite—FM-1 and FM-2 on Terra, FM-3 and FM-4 on Aqua, and FM-6 on NOAA-20—and refer to each group by respective satellite name hereafter. From the grouping, we compared radiance measurements from each satellite's CERES instruments individually, as well as collectively, to those from CTIM. For our comparison, we determined relative difference as

$$\frac{CERES\ Weighted\ Mean\ Radiance - CTIM\ Radiance}{CTIM\ Radiance} \times 100\% \quad (6)$$

where for every match with CTIM, the CERES footprints within the CTIM footprint were adjusted for clear-sky limb darkening, weighted by the CTIM angular/spatial response function and footprint area ratio, and averaged for a mean radiance, as described in Sect. 4. Figure 14 shows the relative differences between CTIM and CERES on each satellite (top) and the relative differences between CTIM and all CERES instruments aboard all three satellites (bottom). It is important to note that the Aqua dataset was limited in time, as the SSF Level-2 data production stopped on March 21, 2023. Because of this, the Aqua data had significantly fewer matches than Terra and NOAA-20. Both Terra and NOAA-20 individually provided data over the entire CTIM lifetime.

https://doi.org/10.5194/egusphere-2026-2197
Preprint. Discussion started: 23 April 2026
© Author(s) 2026. CC BY 4.0 License.

Terra had 313 matches with CTIM with a relative difference of -1.27% ± 0.45%. Aqua had 158 matches with a relative difference of -1.39% ± 0.82%. NOAA-20 had 251 cases with a relative difference of -1.20% ± 0.46% (Table 3). Collectively (labeled CERES in Fig. 14 and in Table 3), the three satellites had 722 matches with CTIM with a mean relative difference of -1.27% ± 0.31%. Uncertainties represent the half-width of bootstrapped 95% confidence intervals (10,000 resamples). The standard deviation of the relative differences was 4.23%. The negative mean relative difference indicates that CTIM observed higher radiances than CERES on average. Linear regression of all 722 cases yielded a coefficient of determination of $R^2 = 0.948$ (Fig. 15), indicating a high degree of correlation between CTIM radiances and CERES mean radiances for the CTIM–CERES matches. The observed spread (σ = 4.23%) was still likely influenced by differences in viewing geometry and scene variability within the large CTIM footprint, rather than by instrument calibration uncertainty. For reference, CTIM measured TSI with an uncertainty of 0.017% (Flynn, et al., 2024), and CERES longwave radiances are assumed to have a calibration uncertainty of 0.75% (k=1) (Loeb et al., 2018a). The CTIM radiance uncertainty budget (Table 2) shows total standard uncertainties of 1.65% and 1.80% (k=1) for shortwave and longwave, respectively, dominated by solid angle uncertainty. Note that CTIM was designed for measuring solar irradiance with its narrow 0.5º divergence, at an uncertainty of less than 0.02%. Intentionally designing the optical system to accommodate Earth-viewing with a larger spread in direction of outgoing radiation would substantially reduce uncertainty in future ERB radiance measurements. The comparisons shown in Fig. 14 and Table 3 show that CTIM and CERES agree to well within their respective uncertainties and that the CERES instruments used in this study agree with one another within less than 0.2%.

Source	Shortwave (%)	Longwave (%)
Detector reflectance	0.07	0.7
Detector power	0.008	0.008
Non-equivalence	0.13	0.13
Noise	0.15	0.15
Dark signal	0.19	0.19
Solid angle	1.63	1.63
Total	*1.65*	*1.80*

Table 2: CTIM radiance standard uncertainties (k=1). The uncertainty was dominated by the uncertainty in the solid angle and secondarily the reflectance. Both could be reduced for future instruments by implementing minor design changes and additional lab calibrations.

https://doi.org/10.5194/egusphere-2026-2197
Preprint. Discussion started: 23 April 2026
© Author(s) 2026. CC BY 4.0 License.

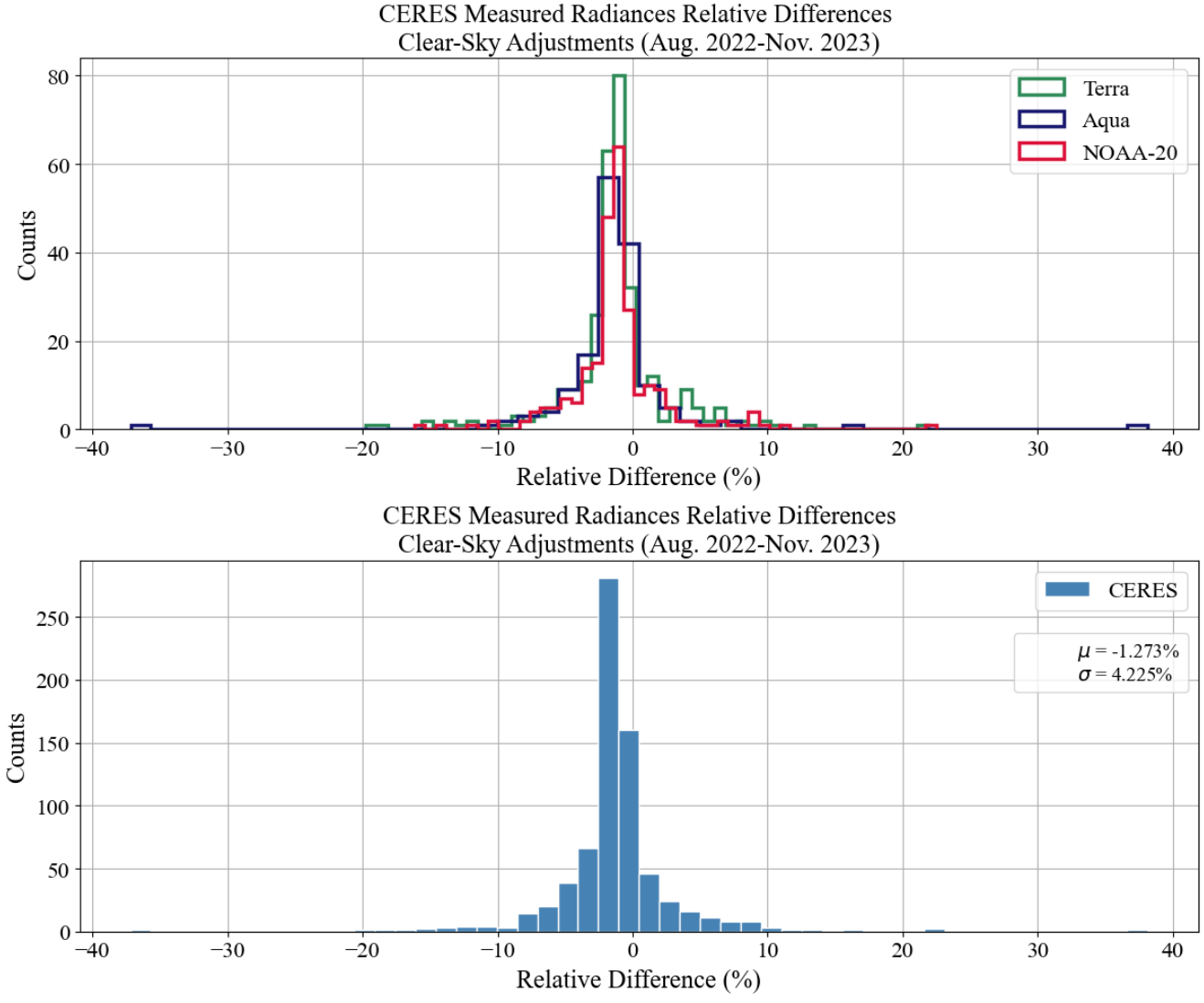

Figure 14: Relative difference histograms between CTIM and CERES measured longwave radiances for 722 matches. Top: Relative differences between CTIM and CERES radiance measurements for Terra, Aqua, and NOAA-20. Bottom: Relative differences between CTIM and CERES, where CERES represents the collective data from CERES aboard Terra, Aqua, and NOAA-20.

https://doi.org/10.5194/egusphere-2026-2197
Preprint. Discussion started: 23 April 2026
© Author(s) 2026. CC BY 4.0 License.

Satellite	Relative Difference	Matches with CTIM
Terra	-1.273% ± 0.451%	313
Aqua	-1.394% ± 0.821%	158
NOAA-20	-1.198% ± 0.461%	251
CERES	-1.273% ± 0.309%	722

Table 3: Relative differences for each CERES satellite compared to CTIM, including the number of matching CTIM footprints per satellite based on our matching methods.

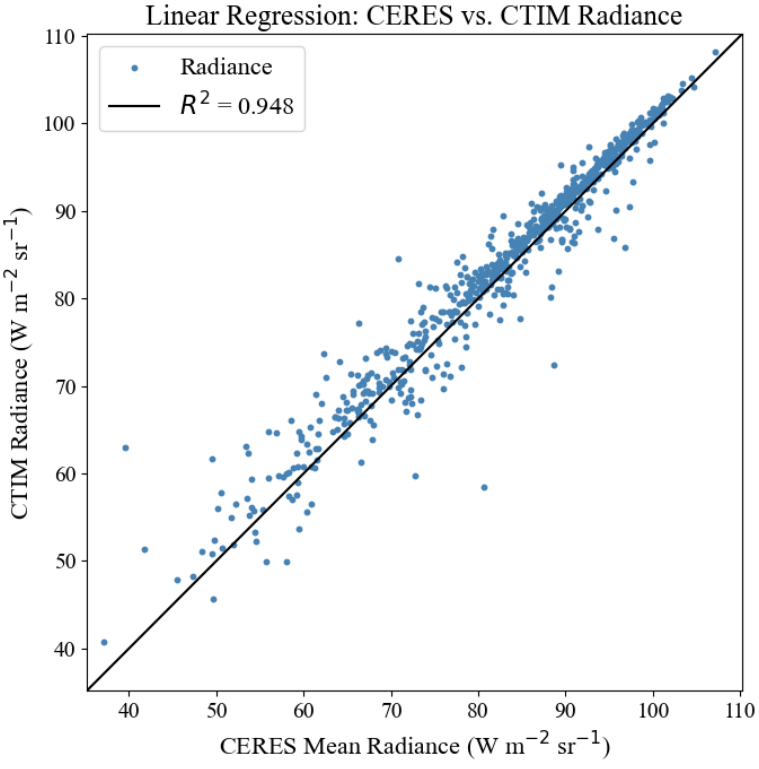

Figure 15: Linear regression of CERES (represented by Terra, Aqua, & NOAA-20) vs. CTIM radiances for 722 matches with clear-sky adjustments. The coefficient of determination (R^2) was 0.948, indicating a strong relationship between CTIM radiances and the CERES mean radiances for every CTIM–CERES match.

https://doi.org/10.5194/egusphere-2026-2197
Preprint. Discussion started: 23 April 2026
© Author(s) 2026. CC BY 4.0 License.

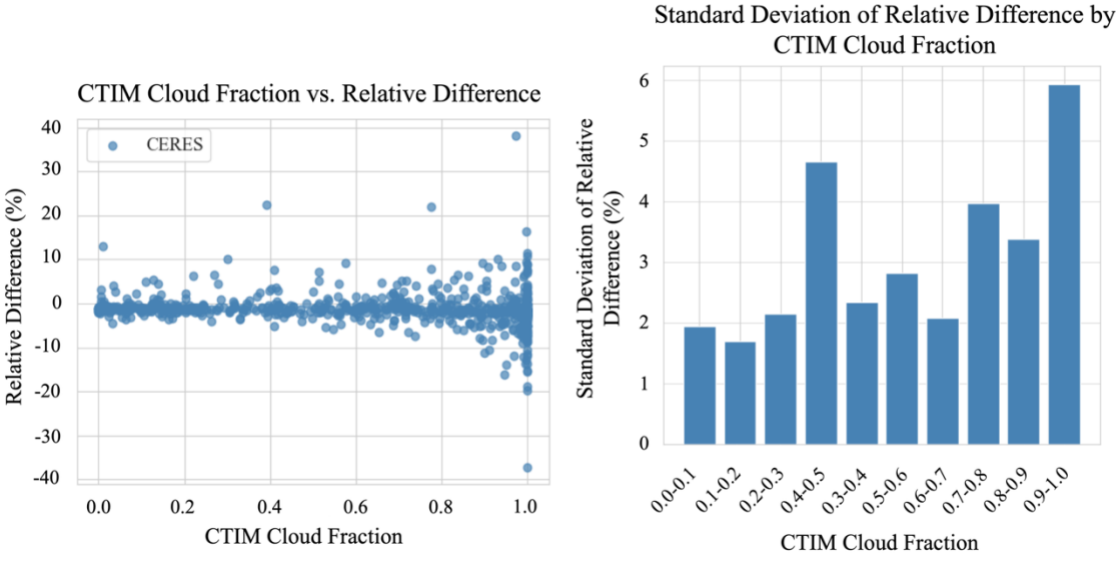

Figure 16: Total cloud compared to radiance relative differences for all 722 matches. Left: The relative difference of CERES and CTIM radiance by CTIM cloud fraction (average cloud fraction from corresponding matching CERES footprints within a CTIM footprint). Right: The standard deviation of relative differences binned by CTIM cloud fraction. As CTIM cloud fraction increased, the standard deviation of relative difference increased, except for the 0.4-0.5 bin, which had an outlier in relative difference shown in the left figure.

Note that the spread in variation between CTIM and CERES decreased as the radiance values increased (Fig. 15). The spread in the lower radiance values could indicate the presence of clouds (colder scenes). Clouds may complicate CTIM–CERES comparisons because the CERES more oblique viewing angles traverse longer paths through cloud layers than the CTIM nadir view. Although CTIM measures radiance over approximately 20 degrees from nadir with decreasing weight at increasing angles, the two instruments still sample cloud layers along meaningfully different path lengths, introducing sensitivity to cloud optical depth, vertical structure, and temperature profile. Figure 16 supports the notion that clouds play a role in the spread in radiance in the CTIM–CERES matches. There is a greater spread in relative difference with increased cloud fraction within the CTIM footprint, as determined by averaging cloud fraction from corresponding matching CERES footprints. The standard deviation of relative difference binned by CTIM cloud fraction (Fig. 16, right) supports the hypothesis that the presence of clouds viewed at different geometries may be responsible, at least in part, to the spread in our results, which was only negligibly reduced after clear-sky limb-darkening adjustments (Fig. 14).

https://doi.org/10.5194/egusphere-2026-2197
Preprint. Discussion started: 23 April 2026
© Author(s) 2026. CC BY 4.0 License.

7 Conclusions

Predicting Earth's future climate requires long-term continuous and accurate ERB observations (Dewitte & Clerbaux, 2017; Loeb et al., 2016; Loeb et al., 2024; Su et al., 2020). Further, ensuring a seamless multidecadal CDR requires overlap between successive ERB instruments from space. Currently, sustaining the ERB record faces increasing challenges. The CERES instruments aboard Terra and Aqua are scheduled to end science data collection in 2026 and Suomi-NPP in 2027, leaving only NOAA-20 to overlap with Libera when it launches in 2027. Loeb et al. (2024) quantify the risk of a data gap: The probability of a data gap is less than 5% through January 2027 but increases to 33% in 2028 and a 60% probability in 2035. The greatest reduction in data gap probability would likely result from launching a new ERB mission in addition to Libera. Emphasizing the significant value of a launch in the near term in addition to Libera in 2027, Loeb et al. (2024) concluded that launching an ERB mission in 2026 would limit the gap probability to 15% through 2035, a launch in 2027 would raise this probability to 30%, and a launch in 2030 would keep it below 41% over the same period. Such projected gap probabilities highlight the value of supplementing the observational record with low-cost, rapidly deployable platforms like CubeSats, which could provide a buffer against future continuity losses.

Implementation of novel CubeSat technology for ERB observation will lower the gap risk in ERB records by increasing synergistic opportunities with complementary systems at lower costs. The compact dimensions of a CubeSat reduce the launch cost, facilitating increased launch opportunities. While the design robustness (compared to large platforms) of CubeSats is limited by size, multiple independent instruments with lower individual reliability can collectively match the dependability of a single large, highly reliable platform. For example, three independent CubeSats with a three-year on-orbit survival probability of 63% collectively raise the success probability to 95% (Harber et al., 2019). Lower costs and risks for launch increase the possibility of low-cost operational missions that implement a constellation of independent instruments to complement large platforms. Gristey et al. (2017) demonstrated that a large, theoretical constellation of wide-field-of-view (WFOV) broadband radiometers could deliver unprecedented temporal and spatial sampling for improving ERB measurements. Wong et al. (2018), however, contend that achieving the necessary calibration and intercalibration across nonscanner instruments for climate-quality data remains a major challenge.

Still, the rapid advancement and miniaturization in technology and the rising accessibility of small satellite platforms create viable pathways for CubeSat constellations for ERB observations, complementary to larger missions. One recent example of exploring this notion is the Uvsq-Sat and Inspire-Sat CubeSats, which are part of the first European constellation demonstrator dedicated to the design and implementation of a heterogeneous WFOV constellation for complementing ERB measurements made by CERES (Meftah et al., 2025). Another example is the RAVAN CubeSat technology demonstration, which represented an important step for ERB measurements from a CubeSat (Swartz, et al., 2019). The BABAR-ERI 12U

https://doi.org/10.5194/egusphere-2026-2197
Preprint. Discussion started: 23 April 2026
© Author(s) 2026. CC BY 4.0 License.

CubeSat could demonstrate inexpensive, low-risk measurements of ERB in parallel with CERES and Libera (Coddington et al., 2025). Similarly, CTIM demonstrates a potential pathway for CubeSat implementation in ERB observations from space.

We report opportunistic longwave radiance Earth observations from the CTIM CubeSat and compare them to Earth radiance observations from CERES, the instruments that have maintained the world's longest continuous ERB record. We created an algorithm for matching CTIM and CERES in space and time. We conducted over 500 MODTRAN simulations to generate the limb-darkening adjustments factors for clear-sky scenes and accounted for CERES footprint areas off nadir. In the fifteen months of CTIM Earth observations, we found the relative difference between CTIM and CERES longwave radiances to be -1.27% ± 0.31% with a 0.948 coefficient of determination for 722 matches. These results show agreement between the two different platforms within their respective uncertainties. Notably, the CTIM optical system was not designed for Earth-viewing; an optical system designed specifically for Earth-viewing could reduce radiance uncertainty to within an order of magnitude of the solar irradiance uncertainty.

This study suggests that leveraging novel CubeSat technology to demonstrate CTIM opportunistic Earth-observing applications may complement heritage ERB missions and reduce the risk of gaps in future ERB observations from space. Moreover, this work provides a potential pathway for the direct measurement of Earth's energy imbalance using the same systems for Earth and Sun measurements. The routine inclusion of Earth-viewing capabilities in future TSI instrument designs emerges as a natural extension of this work, with the potential to meaningfully contribute to ERB observation continuity, maximize scientific utility, and reduce dependence on dedicated large-scale missions.

Code and data availability

The algorithm developed for this paper is freely available on GitHub (https://github.com/mckenziehawkins/CTIM-CERES). The CERES SSF Level-2 data are available at (https://ceres.larc.nasa.gov/data/), and the CTIM data are found within the previously mentioned GitHub repository.

Supplement link

The link to the supplement will be included by Copernicus, if applicable.

https://doi.org/10.5194/egusphere-2026-2197
Preprint. Discussion started: 23 April 2026
© Author(s) 2026. CC BY 4.0 License.

Author contributions

MH led the study, developed the matching algorithm, conducted the MODTRAN simulations, and prepared the manuscript. PP supervised the study and contributed to its conceptualization. MW contributed to the conceptualization and preliminary work and assisted with algorithm development. DH served as principal investigator of the CTIM instrument, providing data and instrument expertise essential to the study. MV contributed to the conceptualization and preliminary work of the study. PP and DH contributed to the review and editing of the manuscript.

Competing interests

None of the authors of this paper have competing interests.

Acknowledgements

The authors would like to thank Bruce Kindel for discussions about the MODTRAN software. The authors would like to thank Odele Coddington, Jake Gristey, and Sebastian Schmidt for reading early drafts and providing feedback. The authors would also like to thank the reviewers who provided thoughtful comments on our manuscript, which significantly improved our study.

Financial support

This research was funded by the Libera project under NASA Contract 80LARC20D0006 and through the research grant from the NASA Earth Science Technology Office (ESTO) 80NSSC18K1502.

Review statement

The review statement will be added by Copernicus Publications listing the handling editor as well as all contributing referees according to their status anonymous or identified.

References

Barkstrom, B. R. & Smith, G. L. (1986). The Earth Radiation Budget Experiment: Science and implementation. *Review of Geophysics, 24*(2), 379-390. https://doi.org/10.1029/RG024i002p00379

https://doi.org/10.5194/egusphere-2026-2197
Preprint. Discussion started: 23 April 2026
© Author(s) 2026. CC BY 4.0 License.

Berk, A., Conforti, P., Kennett, R., Perkins, T., Hawes, F., & van den Bosch, J. (2014). MODTRAN® 6: A major upgrade of the MODTRAN® radiative transfer code. *In Proceedings of the 6th Workshop on Hyperspectral Image and Signal Processing: Evolution in Remote Sensing (WHISPERS)* (pp. 1–4). IEEE. https://doi.org/10.1109/WHISPERS.2014.8077573

CERES Surface Type IDs. (2025, May 27). *CERES general product information*. NASA Langley Research Center. https://ceres.larc.nasa.gov/data/general-product-info/#ceres-surface-type-ids

Clerbaux. N., Akkermans, T., Baudrez, E., Valazquez Blazquez, A., Moutier, W., Moreels, J., & Aebi, C. (2020). The Climate Monitoring SAF outgoing longwave radiation from AVHRR. *Remote Sens., 12*(6), 929. https://doi.org/10.3390/rs12060929

Coddington, O., Harber, D., Pilewskie, P., Richard, E., & Patton, T. (2025). Analysis of the long-term stability of TSI instruments using Allan Deviation and the generation of a new TSI composite. *Earth and Space Science, 12*. https://doi.org/10.1029/2025EA004373

Coddington, O., Straatsma, C., Drake, G., Tyagi, K., Stephens, M., Yung, C., Tomlin, N., Lehamn, J., Bollendonk, C., Buedel, P., Catani, K., Cervelli, B., Chanthavong, S., Crowfoot, T., Dean, G., Erickson, D., Frank, W., Fyhrie, A., Gathright, D.,… Zagorec-Marks, W. (2025). The Black Array of Broadband Absolute Radiometers Earth Radiation Imager: Science requirements, instrument designs, and concept of operations. *Adv. Atmos. Sci.,* 43, 336-360. https://doi.org/10.1007/s00376-025-5049-6

Dewitte, S. & Clerbaux, N. (2018). Decadal changes of Earth's outgoing longwave radiation. *Remote Sens., 10*(10), 1539. https://doi.org/10.3390/rs10101539

Flynn, S., Bershenyi, G., Boyle, B., Harber, D., Cervelli, B., Genarri, S., Fyhrie, A., Pickerill, A., Sprunk, J., Bryant, K., Folgmann, C. (2024). CTIM operational lessons learned and successes. In *Proceedings of the 38th Annual Small Satellite Conference*. Utah State University. https://digitalcommons.usu.edu/cgi/viewcontent.cgi?article=5861&context=smallsat

Forster, P. T., Storelvmo, K., Armour, W., Collins, J., Dufresne, D., Frame, D. J., Lunt, T., Mauritzen, M. D., Palmer, M., Watanabe, M., Wild, M., & Zhang, H. (2021). The Earth's energy budget, climate feedbacks, and climate sensitivity. In V. Masson-Delmotte et al. (Eds.), *Climate change 2021: The physical science basis* (pp. 923–1054). Cambridge University Press. https://doi.org/10.1017/9781009157896.009

https://doi.org/10.5194/egusphere-2026-2197
Preprint. Discussion started: 23 April 2026
© Author(s) 2026. CC BY 4.0 License.

Global Climate Observing System. (2023). *Essential Climate Variables: Earth radiation budget*. World Meteorological Organization. https://gcos.wmo.int/en/essential-climate-variables/earth-radiation-budget

Green, R., & Wielicki, B. A. (1997). Clouds and the Earth's Radiant Energy System (CERES) algorithm theoretical basis document: Convolution of imager cloud properties With CERES footprint point spread function (Subsystem 4.4). https://ceres.larc.nasa.gov/documents/ATBD/pdf/r2_2/ceres-atbd2.2-s4.4.pdf

Gristey, J. J., Chiu, C., Gurney, R. J., Han, S., & Morcrette, C. J. (2016). Determination of global Earth outgoing radiation at high temporal resolution using a theoretical constellation of satellites. *J. Geophys. Res. Atmos., 122*(2), 1114–1131. https://doi.org/10.1002/2016JD025514

Harber, D. M., Castleman, Z., Drake, G., Van Dreser, S., Farber, N., Heuerman, K., Miller, M., Rutkowski, J., Sims, A., Sprunck, J., Straatsma, C., Wanamaker, I., Zheng, W., Kopp, G., Richard, E. C., Pilewskie, P., Tomlin, N., Stephens, M., Yung, C., … Lehman, J. (2019). Compact total irradiance monitor flight demonstration. In C. D. Norton, T. S. Pagano, & S. R. Babu (Eds.), *CubeSats and SmallSats for Remote Sensing III* (p. 12). SPIE. https://doi.org/10.1117/12.2531308

House, F. B., Gruber, A., Hunt, G. E., & Mecherikunn, A. T. (1986). History of satellite missions and measurements of the Earth radiation budget (1957-1984). *Rev. Geophys, 24*(2), 357-77. https://doi.org/10.1029/RG024i002p00357

Jahani, B., Anderson, H., Calbó, J., González, J., & Cermak, J. (2022). Longwave radiative effect of the cloud-aerosol transition zone based on CERES observations. *Atmos. Chem. Phys., 22,* 1483-1494. https://doi.org/10.5194/acp-22-1483-2022

JPSS Performance Status. (2025, August 18). NOAA office of satellite and product operations. Retrieved January 21, 2026, from https://www.ospo.noaa.gov/operations/jpss/status.html

Loeb, G. G., Kato, S., Loukachine, K., & Manalo-Smith, N. (2005). Angular distribution models for top-of-atmosphere radiative flux estimation from the Clouds and the Earth's Radiant Energy System instrument on the Terra satellite. Part I: Methodology. *J. Atmos. Oceanic Technol., 22*(4), 338-351. https://doi.org/10.1175/JTECH1712.1

Loeb, N. G., Manalo-Smith, N., Su, W., Shankar, M., & Thomas, S. (2016). CERES top-of-atmosphere Earth radiation budget climate data record: Accounting for on-orbit changes in instrument calibration. *Remote Sens., 8*(3), 182. https://doi.org/10.3390/rs8030182

https://doi.org/10.5194/egusphere-2026-2197
Preprint. Discussion started: 23 April 2026
© Author(s) 2026. CC BY 4.0 License.

Loeb, N. G., Doelling, D. R., Wang, H., Su, W., Nguyen, C., Corbett, J. G., Liang, L., Mitrescu, C., Rose, F. G., & Kato, S. (2018a). Clouds and the Earth's Radiant Energy System (CERES) Energy Balanced and Filled (EBAF) top-of-atmosphere (TOA) edition-4.0 data product. *J. Climate, 31*(2), 895-918. https://doi.org/10.1175/JCLI-D-17-0208.1

Loeb, N. G., Doelling, D. R., Kato, S., Su, W., Mlynczak, P. E., & Wilkins, J. C. (2024). Continuity in top-of-atmosphere Earth radiation budget observations. *J. Climate, 37*(23), 6093-6108. https://doi.org/10.1175/JCLI-D-24-0180.1

Loeb, N. G., Priestley, K. J., Kratz, D. P., Geier, E. B., Green, R. N., Wielicki, B. A., Hinton, P. O., & Nolan, S. K. (2001). Determination of unfiltered radiances from the Clouds and the Earth's Radiant Energy System instrument. *J. Appl. Meteor. Climatol., 40*(4), 822-835. https://doi.org/10.1175/1520-0450(2001)040<0822:DOURFT>2.0.CO;2

Loeb, N. G., Su, W., Doelling, D. R., Wong, T., Minnis, P., Thomas, S., & Miller, W. F. (2018b). Earth's top-of-atmosphere radiation budget. *Comp. Remote Sens., 5*, 67–84. Elsevier. https://doi.org/10.1016/B978-0-12-409548-9.10367-7

Meftah, M., Dufour, C., Keckhut, P., Sarkissian, A., & Zhu, P. (2025). Variability and trends in Earth's radiative energy budget from Uvsq-Sat (2021-2024) and CERES observations (2013-2024). *Remote Sens., 17*(16), 2751. https://doi.org/10.3390/rs17162751

Minnis, P., Sun-Mack, S., Smith, Jr., W. L., Trepte, Q. Z., Hong, G., Chen, Y., Yost, C. R., Chang, F-L., Smith, R. A., Heck, P. W., & Yang, P. (2023). VIIRS edition 1 cloud properties for CERES, part 1: Algorithm adjustments and results. *Remote Sens., 15*(3), 578. https://doi.org/10.3390/rs15030578

National Academies of Sciences, Engineering, and Medicine. (2018). Thriving on our changing planet: A decadal strategy for Earth observation from space. Washington, DC: The National Academies Press. https://doi.org/10.17226/24938

Parkinson, C. L., Ward, A., & King, M. D. (Eds.). (2006). *Earth science reference handbook: A guide to NASA's Earth science program and Earth observing satellite missions*. National Aeronautics and Space Administration (NASA), Goddard Space Flight Center.

Pilewskie, P., Hakuba, M., & Libera Science Team. (2022, October 12-14). *Libera overview and mission status* [Conference Presentation]. 2022 Earth Radiation Budget Workshop, MPI, Hamberg, Germany. Chrome-extension://efaidnbmnnnibpcajpcglclefindmkaj/https://ceres.larc.nasa.gov/documents/STM/2022-10/Pilewskie_CERES_Libera_science_meeting12oct22.pdf

https://doi.org/10.5194/egusphere-2026-2197
Preprint. Discussion started: 23 April 2026
© Author(s) 2026. CC BY 4.0 License.

Priestley, K., Thomas, S., & Smith, G. L. (2018). Enabling continuity of Earth radiation budget measurements initial results. IGARSS 2018 - 2018 IEEE International Geoscience and Remote Sensing Symposium, Valencia, Spain, 2018, pp. 7739-7742, https://doi.org/10.1109/IGARSS.2018.8519268.

Smith, G. L., Manalo-Smith, N., & Avis, L. M. (1994). Limb-darkening models from along-track operation of the ERBE scanning radiometer. *J. Appl. Meteor. Climatol., 33*(1), 74-84. https://doi.org/10.1175/1520-0450(1994)033<0074:LDMFAT>2.0.CO;2

Stephens, G. L., Li, J., Wild, M., Clayson, C., Loeb, N. Kato, S., L'Ecuyer, T., Stackhouse, Jr., P.W., Lebsock, M., Andrews, T. (2012). An update on Earth's energy balance in light of the latest global observations. *Nature Geosci.,* 5(10), 691-696. https://doi.org/10.1038/NGEO1580

Su, W., Liang, L., Wang, H., & Eitzen, Z. A. (2020) Uncertainties in CERES top-of-atmosphere fluxes caused by changes in accompanying imager. *Remote Sens., 12*, 2040. https://doi.org/10.3390/rs12122040

Swartz, W. H., Lorentz, S. R., Papadakis, S. J., Huang, P. M., Smith, A. W., Deglau, D. M., Yu, Y., Reilly, S. M., Reilly, N. M., & Anderson, D. E. (2019). *Remote Sens., 7*(11), 796. https://doi.org/10.3390/rs11070796

Taylor, P. C., Itterly, K. F., Corbett, J., Bucholtz, A., Sejas, S., Su, W., Doelling, D., & Kato, S. (2022). A comparison of top-of-atmosphere radiative fluxes from CERES and ARISE. *J. Geophys. Res. Atmos.*, *127*(24), e2022JD037573. https://doi.org/10.1029/2022JD037573

Tomlin, N. A., Yung, C. S., Castleman, Z., Denoual, M., Drake, G., Farber, N., Harber, D., Heuerman, K., Kopp, G., Passe, H., Richard, E., Rutkowski, J., Sprunck, J., Stephens, M., Straatsma, C., Van Dreser, S., Vayshenker, I., White, M., G., Woods, S. I.,… Lehman, J.H. (2020). Overview of microfabricated bolometers with vertically aligned carbon nanotube absorbers. *AIP Advances, 10*(5), 055010. https://doi.org/10.1063/5.0004025

Vonder Haar, T. H., & Suomi, V. E. (1971). Measurements of the Earth's radiation budget from satellites during a five-year period. Part I: extended time and space means. *J. Atmos. Sci., 28*(3). https://doi.org/10.1175/1520-0469(1971)028<0305:MOTERB>2.0.CO;2

von Schuckmann, K., Palmer, M. D., Trenberth, K. E., Cazenave, A., Chambers, D., Champollion, N., Hansen, J., Loeb, N., Mathieu, P. -P., Meyssignac, B., & Wild, M. (2016). An imperative to monitor Earth's energy imbalance. *Nature Clim. Change, 6*, 138-144. https://doi.org/10.1038/nclimate2876

https://doi.org/10.5194/egusphere-2026-2197
Preprint. Discussion started: 23 April 2026
© Author(s) 2026. CC BY 4.0 License.

Von Schuckmann, K., Minière, A., Gues, F., Cuesta-Valero, F. J., Kirchengast, G., Adusumilli, S., Straneo, F., Ablain, M., Allan, R. P., Barker, P. M., Beltrami, H., Blazquez, A., Boyer, T., Cheng, L., Church, J., Desbruyeres, D., Dolman, H., Domingues, C. M., García-García, A., … Zemp, M. (2023). Heat stored in the Earth system 1960–2020: Where does the energy go? *Earth Syst. Sci. Data*, 15(4), 1675–1709. https://doi.org/10.5194/essd-15-1675-2023

Wielicki, B. A., Barkstrom, B. A., Harrison, E. F., Lee III, R. B., Smith, G. L., Cooper, J. E. (1996). Clouds and the Earth's Radiant Energy System (CERES): An Earth observing system experiment. *Bull. Amer. Meteor. Soc., 77*(5), 858-868. https://doi.org/10.1175/1520-0477(1996)077<0853:CATERE>2.0.CO;2

Wong, T., Smith, G. L., Kato, S., Loeb, N. G., Kopp, G., & Shrestha, A. K. (2018). On the lessons learned from the operations of the ERBE nonscanner instrument in space and the production of the nonscanner TOA radiation budget data set. *IEEE Transactions on Geoscience and Remote Sensing*, *56*(10), 5936–5947. https://doi.org/10.1109/TGRS.2018.2828783